

# Large anomalous Hall conductivity in Weyl ferrimagnet $\text{Cs}_2\text{Co}_3\text{S}_4$ predicted by density-functional calculations

Gang Bahadur Acharya,<sup>1,2</sup> Manuel Richter,<sup>2,3</sup> Klaus Koepernik,<sup>2</sup> and Madhav Prasad Ghimire<sup>1,2,\*</sup>

<sup>1</sup>*Central Department of Physics, Tribhuvan University, Kirtipur, 44613, Kathmandu, Nepal*

<sup>2</sup>*Leibniz-IFW Dresden, Helmholtzstr. 20, 01069 Dresden, Germany*

<sup>3</sup>*Dresden Center for Computational Materials Science (DCMS), TU Dresden, D-01062 Dresden, Germany*

The identification of topological Weyl semimetals has recently gained considerable attention. Here, we report the results of density-functional theory calculations regarding the magnetic properties, the electronic structure, and the intrinsic anomalous Hall conductivity of the title compound, which was synthesized already 50 years ago but received little attention, hitherto. We found  $\text{Cs}_2\text{Co}_3\text{S}_4$  to be a ferrimagnetic half-metal with a total spin magnetic moment of about  $3 \mu_B$  per formula unit. It shows energy band gap of 0.36 eV in the majority-spin channel and a pseudo-gap at the Fermi level in the minority-spin channel. We identified several sets of low-energy Weyl points and traced their dependence on the direction of magnetization. The intrinsic anomalous Hall conductivity is predicted to reach a magnitude up to  $500 \Omega^{-1}\text{cm}^{-1}$ , which is comparable to values obtained in other celebrated Weyl semimetals.

## I. INTRODUCTION

Dirac semimetals, Weyl semimetals (WSMs), nodal line semimetals, and triple point semimetals are the four main types of topological semimetals. This classification is based on the node distribution in the crystal momentum  $k$  space and the related band degeneracy. [1–15] If two non-degenerate bands cross or touch in a single, separated point in  $k$ -space, this is called a Weyl point (WP). WPs are topologically protected and are robust against small perturbations [16] and they exist in pairs with opposing chiral charges. [17–19] Non-degenerate bands, which are required for the existence of WPs, are present if inversion symmetry (IS) or time reversal symmetry (TRS) or both are broken.

Most of the recent research on WSMs is focused on non-magnetic compounds, where IS is broken such as in the TaAs family [20–23], in  $\text{WTe}_2$  [24, 25], in  $\text{MoTe}_2$  [26–28], in  $\text{Mo}_x\text{W}_{1-x}\text{Te}_2$  [29–32], in  $\text{TaIrTe}_4$  [33, 34], etc. These materials show intrinsic electronic characteristics with potential for future electronic applications. For instance, the gapless band structure can be useful for broadband photodetectors [11, 35], the spin momentum locking of Fermi arcs for spintronics [36], and the helical nature of surface electrons for topological qubits. [12, 37, 38]

Studies on magnetic WSMs are still less frequent in comparison to those on non-magnetic WSMs. A pyrochlore iridate,  $\text{Y}_2\text{Ir}_2\text{O}_7$ , was the first theoretically predicted magnetic WSM [39], followed by  $\text{HgCr}_2\text{Se}_4$ ,  $\text{Ti}_2\text{MnAl}$ ,  $\text{Co}_3\text{Sn}_2\text{S}_2$ ,  $\text{YbMnBi}_2$ ,  $\text{Co}_2\text{MnGa}$ ,  $\text{Mn}_3\text{Sn}/\text{Mn}_3\text{Ge}$ ,  $\text{GdPtBi}$  [40–48], as well as certain Co-based Heusler compounds predicted to host a TRS-breaking Weyl phase. [49–51]

In recent years, magnetic WSMs are receiving more attention due to several advantages. For instance, the

position of Weyl points in the reciprocal space and their energy can be tuned by rotating the magnetization. [44] In this way, the related intrinsic anomalous Hall conductivity and the anomalous Nernst conductivity are also tuned. Further, in WSMs where both IS and TRS are broken, application of an external magnetic field can rotate the magnetization into a general direction such that the Shubnikov group contains only the identity element. In such a case, pairs of Weyl points split in energy, giving access to chiral electromagnetic responses. [52]

The present investigation is devoted to the magnetic compound  $\text{Cs}_2\text{Co}_3\text{S}_4$ . This compound was first synthesized and characterized by x-ray powder diffraction in 1972. [53] Somewhat later, single crystals of the title compound were prepared by Bronger *et al.* [54], henceforth referred to as BHM. The structure and magnetic state of these single crystals were characterized by x-ray diffraction (XRD) and neutron diffraction (ND) in the same work. Though the compound is known for half of a century, there are no further investigations on  $\text{Cs}_2\text{Co}_3\text{S}_4$  published, to the best of our knowledge. This lack of information motivated us to perform a systematic research on the magnetic ground state and electronic properties of  $\text{Cs}_2\text{Co}_3\text{S}_4$  on the basis of density functional theory (DFT). We found a ferrimagnetic ground state which is (almost) half metallic and, at the same time, semi-metallic. As a consequence, we could characterize the compound as a WSM and evaluated the intrinsic contribution to the anomalous Hall conductivity (AHC).

## II. CRYSTAL STRUCTURES AND COMPUTATIONAL DETAILS

$\text{Cs}_2\text{Co}_3\text{S}_4$  crystallizes in a body centered orthorhombic Bravais lattice with the centrosymmetric space group  $Ibam$  (SG 72) and two formula units per primitive unit cell. Experimental lattice parameters and atomic positions were determined both by XRD and by ND. While

\* madhav.ghimire@cdp.tu.edu.np

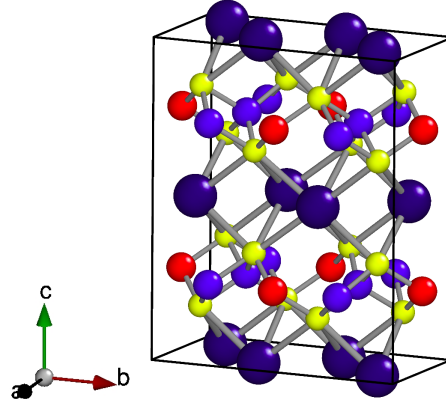


FIG. 1. Crystal structure of  $\text{Cs}_2\text{Co}_3\text{S}_4$  in the conventional elementary cell. Violet (blue, red, yellow) balls denote Cs (Co(I), Co(II), S) atoms.

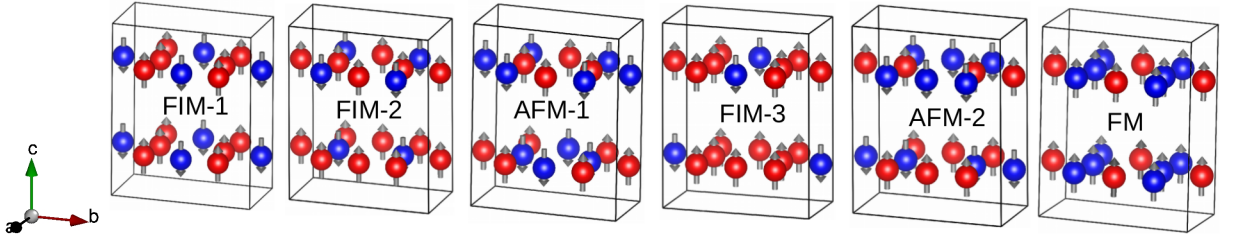


FIG. 2. Considered spin configurations. From left to right, different ferrimagnetic (FIM), antiferromagnetic (AFM), and ferromagnetic (FM) arrangements are depicted in ascending order of their energy according to our calculations using experimental room-temperature lattice parameters. Only Co atoms are shown. Different colors denote different spin orientations.

the ND data were obtained at a temperature of 4.2 K, XRD was presumably performed at room temperature [54].

The experimental lattice parameters obtained by room-temperature XRD are  $a = 5.712$  Å,  $b = 11.231$  Å, and  $c = 13.879$  Å. According to the same experiment, Cs and S atoms occupy the 8j and 16k sites at (0.2336, 0.1205, 0) and at (0.2233, 0.3669, 0.1589), respectively, while the Co atoms occupy the 8g sites, denoted as Co(I), at (0, 0.2319, 0.25) and the 4b sites, denoted as Co(II), at (0.5, 0, 0.25), see BHM.

The structure is shown in Fig. 1. The Cs atoms are centered within distorted cubes of S atoms, and the Co atoms are surrounded by S tetrahedra. The related shortest bond lengths amount to 3.54 Å for Cs - S, 2.31 Å for Co(I) - S, and 2.34 Å for Co(II) - S.

The experimental lattice parameters obtained by low-temperature ND amount to  $a = 5.663$  Å,  $b = 11.160$  Å and  $c = 13.708$  Å. They are somewhat smaller than the related room-temperature parameters, in accordance with a positive thermal expansion coefficient. Atomic site positions obtained by ND are Cs-8j (0.234, 0.115, 0), S-16k (0.814, 0.369, 0.14), Co(I)-8g (0, 0.235, 0.25), and Co(II)-4b (0.5, 0, 0.25). These positions agree well with those determined by XRD with the exception of the sulfur position. The latter results in a Cs-S interatomic distance of 1.98 Å, which is only somewhat more than half of the expected value of about 3.6 Å. Thus, we

consider the ND-value of the S-16k atomic position as incorrect and use the XRD atomic positions in all DFT calculations.

The DFT calculations were performed with the full-potential local orbital code (FPLO), [55] version 18.00-52. The standard generalized gradient approximation (GGA) based on the parameterization by Perdew, Burke, and Ernzerhof (PBE) [56] was used for the exchange-correlation potential. Local or semi-local approximations to DFT like GGA suffer from an incomplete description of orbital magnetism that stems from orbital-dependent self-interaction. [57] For this reason, so-called orbital polarization corrections (OPC) in the flavor suggested by Nordström *et al.* [58] were applied in a part of the calculations.

With an aim to check the order of magnetic states, an additional set of calculations was performed with the WIEN2k code which is based on the full-potential linearized augmented plane wave method [59]. For this, we use the Yukawa-screened (YS) hybrid functional YS-PBE0 [60] with  $\alpha = 0.25$  (Hartree-Fock exchange parameter), and  $\lambda = 0.165$  (screening parameter) that give rise to results similar to the HSE06 functional. Other parameters were chosen similar to FPLO calculations.

A linear tetrahedron method with Blöchl corrections was applied for the integrations in reciprocal space. The related  $k$ -mesh contained  $12 \times 12 \times 12$  points in the Brillouin zone for the self-consistent calculations and was

refined to  $20 \times 20 \times 20$  points for the evaluation of band structures and densities of states (DOS) shown in Fig. 3.

Self-consistent calculations were conducted in both scalar relativistic and four component full relativistic modes of FPLO. In the full relativistic mode that includes spin-orbit coupling in all orders, the direction of magnetization was fixed by a global setting of the spin quantization axis. Those calculations were Co atoms at the same Wyckoff position were considered to carry magnetic moments with different orientation, see Fig. 1, were performed in space group  $I222$  (SG 23). The fixed spin moment method (FSM) [61] was applied to force a zero total spin moment for antiferromagnetic (AFM) arrangements.

Maximally projected Wannier functions [62] were produced from self-consistent full relativistic DFT band structures using the PYFPLO module of the FPLO code, version 18.00-52. The localized Wannier basis consists of Cs [5p, 6s], Co [3d, 4s], and S [3p, 3s] orbitals, i.e., a total of 168 orbitals. To map the Wannier model, the same  $k$ -mesh as in the self-consistent calculations was chosen. The generated Wannier Hamiltonians were used to interpolate the band structure at a  $k$ -mesh of  $40 \times 40 \times 40$  points and to search Weyl points with the help of the abovementioned PYFPLO module. The search was limited to the Wannier bands 129-131, counted in ascending order, as lower bands at the Weyl node, see Fig. 3(b).

In the presence of spin-orbit interaction, nodal lines (NL) can only exist on simple mirror planes [63]. We confirmed the presence of NLs by calculating the Berry phase on a closed loop containing the NL. See also the discussion of the gauge choice for link variables in the Appendix.

The  $k$ -space integrations to evaluate the anomalous Hall conductivity were carried out with a mesh of  $200 \times 200 \times 200$  points.

### III. RESULTS AND DISCUSSION

#### A. MAGNETIC GROUND STATE

We started our calculations with a search for the stable magnetic ground state of  $\text{Cs}_2\text{Co}_3\text{S}_4$ .

Based on ND data, a collinear antiferromagnetic (AFM) order was suggested in BHM to be the stable magnetic state at 4.2 Kelvin. In this state, four of the Co(I) sites show a spin orientation opposite to the spin orientation of the four other Co(I) sites and two of the Co(II) sites show a spin orientation opposite to the spin orientation of the two other Co(II) sites (state AFM-1 in Fig. 2). Permutation of the spin orientations of these four groups of sites yields eight different combinations. Two of the combinations are equivalent by symmetry to other combinations. We investigated the six remaining combinations, shown in Fig. 2 which includes ferromagnetic (FM), two different AFM, and three ferrimagnetic (FIM) arrangements.

Table I compiles the relative total energies and spin magnetic moments, obtained by means of calculations in a scalar relativistic mode and using both low-temperature ND and room-temperature XRD lattice parameters. Different from the experimental result, the arrangement FIM-1 is found to be the lowest-energy state both within GGA and hybrid functional YS-PBE0 [60]. However, both FIM-2 and the experimental ground state AFM-1 are further low-energy solutions with energies of 3 meV per atom or less above the computed ground state. All other considered arrangements have much higher total energies.

In order to make sure that the obtained solutions with atomic spin moments of about  $2 \mu_B$  are the only stable solutions of the given arrangements, we performed two tests. First, FSM calculations were done for the case of FM order. They showed that there is no other (meta)stable FM state in the possible range of local moments. Second, calculations for the AFM-1 order were performed with larger than usual initial spin splittings of 4 and  $5 \mu_B$ . Both calculations converged to the same state as obtained with default initial splitting of  $2 \mu_B$  and shown in Table I.

The question arises why the experimental ground state AFM-1 is found higher in energy than the state FIM-1 in the calculations. To get an idea about a possible reason, we performed additional calculations for the states FIM-1 and AFM-1 with slight doping of 0.1 electrons (holes) per unit cell of 18 atoms. As a result, the original energy difference between FIM-1 and AFM-1 of 36.5 meV (ND lattice parameters) was reduced by 1.3 meV (enhanced by 1.4 meV). This means, a strong electron doping would be needed to change the order of the two states, which would only be possible by significant modification of the stoichiometry in the order of a few percent.

We cannot rule out this possibility, nor can we rule out the applied approximation to the exchange-correlation functional (GGA) to be responsible for the disagreement between calculated and experimental ground states. In any case, the two discussed states are relatively close in energy. Thus, it should be possible to prepare FIM-1 either by appropriate modification of the stoichiometry (improved preparation or intentional electron doping) or by application of a moderate external magnetic field. The latter option would be very interesting, since also the state FIM-2 is close to AFM-1. Thus, a competition between three different phases could occur.

Next, we carried out full relativistic calculations including spin-orbit coupling. Here, we focus on the calculated ground state FIM-1 and on the experimental ground state AFM-1. The results are presented in the upper part of Table II.

By spin-orbit coupling, the total energy depends on the direction of magnetization. Here, we consider the three inequivalent orthorhombic directions  $[1\ 0\ 0]$ ,  $[0\ 1\ 0]$ , and  $[0\ 0\ 1]$ . Among these, the lowest energy is found for the configuration FIM-1 with  $[1\ 0\ 0]$  orientation of the magnetization. In the configuration AFM-1, the low-

TABLE I. Scalar relativistic energies and spin moments. Calculated relative total energies  $E$ , given per primitive unit cell with 18 atoms and local and total spin magnetic moments  $M_s$  for the six considered configurations depicted in Fig. 2. ND and XRD indicate the results obtained by using low-temperature ND and room-temperature XRD lattice parameters, respectively.

Configuration	$E$ [meV/unit cell]			$M_s(\text{Co(I)})$ [ $\mu_B$ ]		$M_s(\text{Co(II)})$ [ $\mu_B$ ]		$M_s(\text{unit cell})$ [ $\mu_B$ ]	
	ND	XRD	XRD	ND	XRD	ND	XRD	ND	XRD
XC-Functional	GGA	GGA	YS-PBE0	GGA	GGA	GGA	GGA	GGA	GGA
FIM-1	0	0	0	2.01	2.11	-1.77	-1.91	5.94	5.99
FIM-2	19.6	20.4	37.5	1.98, -1.67	2.09, -1.82	2.03, 2.05	2.13, 2.16	5.96	6.00
AFM-1	36.5	23.1	52.2	1.87, -1.87	2.00, -2.00	2.00, -2.00	2.14, -2.14	0	0
FIM-3	171	161	150	2.01, 2.04	2.17, -2.20	-1.71, 2.13	-1.80, 2.28	10.87	11.58
AFM-2	157	165	174	1.81, -1.81	1.97, -1.97	1.95, -1.95	2.09, -2.09	0	0
FM	367	388	370	1.92	2.04	1.92	2.04	14.26	14.79

TABLE II. Full relativistic energies, spin and orbital moments. Calculated relative total energies  $E$ , given per primitive unit cell with 18 atoms, and local spin, orbital, and total magnetic moments ( $M_s$ ,  $M_l$ , and  $M_{\text{tot}}$ , resp.) of the Co atoms. The two numbers in each column refer to Co(I) and Co(II). The upper part shows results of full relativistic calculations with different orientations of the magnetization for the configurations FIM-1 and AFM-1, the lower part shows results of full relativistic calculations with orbital polarization correction. Low-temperature ND lattice parameters were used for all calculations.

With s-o					
Configuration	Direction of magnetization	$E$ [meV/unit cell]	$M_s(\text{Co})$ [ $\mu_B$ ]	$M_l(\text{Co})$ [ $\mu_B$ ]	$M_{\text{tot}}(\text{Co})$ [ $\mu_B$ ]
FIM-1	[1 0 0]	0	2.00, -1.76	0.17, -0.14	2.17, -1.90
	[0 1 0]	2.7	2.00, -1.77	0.15, -0.15	2.15, -1.92
	[0 0 1]	2.5	2.00, -1.76	0.16, -0.15	2.16, -1.92
AFM-1	[1 0 0]	37.4	$\pm 1.86, \pm 1.99$	$\pm 0.15, \pm 0.16$	$\pm 2.01, \pm 2.15$
	[0 1 0]	37.7	$\pm 1.86, \pm 1.99$	$\pm 0.14, \pm 0.16$	$\pm 2.00, \pm 2.15$
	[0 0 1]	35.1	$\pm 1.86, \pm 1.99$	$\pm 0.18, \pm 0.18$	$\pm 2.04, \pm 2.17$
With s-o and OPC					
FIM-1	[1 0 0]	0	1.99, -1.76	0.70, -0.47	2.69, -2.23
	[0 1 0]	17.9	2.01, -1.77	0.40, -0.56	2.41, -2.33
	[0 0 1]	11.7	2.01, -1.77	0.46, -0.58	2.47, -2.35
AFM-1	[1 0 0]	46.3	$\pm 1.88, \pm 2.01$	$\pm 0.50, \pm 0.57$	$\pm 2.38, \pm 2.58$
	[0 1 0]	51.7	$\pm 1.86, \pm 1.99$	$\pm 0.44, \pm 0.48$	$\pm 2.30, \pm 2.47$
	[0 0 1]	12.6	$\pm 1.85, \pm 1.96$	$\pm 0.71, \pm 0.80$	$\pm 2.56, \pm 2.76$

est energy is achieved if the magnetization is oriented along [0 0 1]. This is in agreement with the easy axis measured by ND in I. The maximum value of the magnetic anisotropy energy (MAE), which is the energy difference between unlike orientations of the magnetization, amounts to about 2.5 meV per unit cell in both configurations. The total magnetic moments per Co atom are not much enhanced in comparison with the scalar relativistic results, due to the relatively small orbital moments that do not exceed 10% of the spin moments. This finding is at variance with the experimental magnetic moments of about 3.7  $\mu_B$ , obtained by ND in I. We note, however, two important caveats. First, the title system is a (half)metal with a relatively broad Co-d band of about 3 eV, see next section. As such, it is expected that the Co orbital moment is ruled by itinerant behavior and, thus, much smaller than the large-moment limit of the  $d^7$  atomic configuration, 3  $\mu_B$ . Second, there exists a generic problem to define the local moment of atoms in an AFM configuration, since the total moment of the unit cell has to be zero. In the present AFM-1 configuration, Co atoms with antiparallel magnetic moments are less than 2.9 Å away from each other, which is only 15% more than the distance in densely packed metallic Co.

Thus, it is possible to define very different local projections of the magnetization density which add up to the same total magnetization density.

Further, we applied so-called orbital polarization corrections (OPC) to GGA. These corrections improve the compliance of GGA and similar approximations to the exchange-correlation functional of DFT with Hund's second rule. [64] Related results are compiled in the lower part of Table II. We note that the spin magnetic moments are merely unchanged in comparison with those obtained by scalar relativistic or full relativistic calculations without OPC. The orbital magnetic moments, however, are enhanced with respect to the data of the latter calculations by factors between two and four. As a result, the total moments amount up to about 2.7  $\mu_B$ . This value is still significantly below the numbers reported, but much larger than cobalt moments commonly known from other metallic systems. Further, the lowest-energy directions of magnetization remain unchanged by OPC for the two considered configurations: [1 0 0] for the configuration FIM-1 and [0 0 1] for AFM-1. This fact is reassuring since AFM-1 [0 0 1] is the experimental ground state. Here, by applying GGA+OPC, this state is found to be only less than 1 meV per atom higher in energy than the

TABLE III. Location of the symmetry points used in Fig. 3.

point	$k_x[2\pi/a]$	$k_y[2\pi/b]$	$k_z[2\pi/c]$
$\Gamma$	0	0	0
X	0.58469	0	0
L	0.58469	0.17259	0
T	1/2	1/2	0
W	1/2	1/2	1/2
R	1/2	0	1/2
X <sub>1</sub>	0.41531	0	1
Z	0	0	1

state FIM-1 [1 0 0].

We conclude this section by stating that we identify the state FIM-1 [1 0 0] as the ground state of the title compound, treated in relativistic GGA without or with OPC, with exact stoichiometry and free of defects. Since this state is very close in energy to the experimental ground state AFM-1 [0 0 1], we think that it can be obtained either directly by refined sample preparation or by application of a moderate external magnetic field. Thus, our further investigations will be focused on FIM-1.

## B. ELECTRONIC STRUCTURE OF THE GROUND STATE

All results of this and the following sections were obtained by using room-temperature XRD structure data from I.

Fig. 3 (a) shows the total and partial densities of states (PDOS) for the ground state FIM-1 configuration in scalar relativistic mode. Majority and minority spin channels are indicated with up- and down-arrows, respectively. The related scalar relativistic band structure on high-symmetry lines is depicted in Fig. 3 (b) and the positions of the symmetry points are compiled in Table III.

The DOS shows an interesting combination of semi-metallic and covalent features. Sulphur states (green color in the upper panel of Fig. 3(a)) dominate the DOS between about -5 eV and about -3 eV (bonding region), while Co states (lower panel of Fig. 3(a)) dominate between -2 eV and +1 eV (anti-bonding region). Both regions are separated by a covalency gap in the minority spin channel. In the majority spin channel, however, this energy range is occupied by states localized almost exclusively at Co(I) sites.

There is a narrow, separated band with a width of only 0.5 eV in the majority spin channel above the Fermi level. However, the widths of the occupied majority spin band and of the minority spin band around the Fermi level in the Co-dominated anti-bonding region amount to about 3 eV. Thus, the title compound is expected to show itinerant magnetism.

Within the majority spin band, there is a 0.36 eV gap only 14 meV above the Fermi level, see Fig. 3 (a, b). Thus, the system is very close to a half metallic state. This finding is in accordance with the calculated spin

moment of  $5.99 \mu_B$ , which is almost an integer value that would indicate half metallicity in a scalar relativistic approximation. Moreover, a narrow pseudogap of about 80 meV width is present in the minority spin band at  $E_F$ , qualifying  $\text{Cs}_2\text{Co}_3\text{S}_4$  as a semi-metal. The majority spin band has a small hole pocket at point  $\Gamma$ , see Fig. 3 (b), and only two minority spin bands cross the Fermi level. Those bands which feature as highest occupied band in certain regions of the  $k$ -space are indicated in Fig. 3 (b) with their band number (129, 130, or 131). Note that these numbers do not include the 120 semi-core states.

The electronic band structure with spin-orbit coupling is shown in Fig. 3 (c) for the case of magnetization along [1 0 0] (ground state). Due to broken TRS, all bands are non-degenerate almost everywhere in the  $k$ -space. Exceptions are bands on the line W-R, which are at least two-fold degenerate by symmetry, and accidental band degeneracies. The latter may form so-called nodal lines or are isolated Weyl points, which are of special interest for their impact on transport behavior, see below.

Inspection of Fig. 3 (c) shows a number of apparent band crossings. We call these degeneracies “apparent”, as the information provided by Fig. 3 (c) does not allow a final categorization into Weyl points, nodal lines, or gapped states. Those apparent crossings that take place between bands  $n$  and  $n + 1$  close to the Fermi level,  $n = \{129, 130, 131\}$ , are marked in Fig. 3 (c) by numbers 1 to 5 and will be investigated in the following section.

If the magnetization is rotated by, e.g., application of an external magnetic field, the band structure changes due to spin-orbit coupling. This means that also the positions and energies of Weyl points depend on the direction of magnetization, and pairs of Weyl points may even annihilate or emerge. [44] This effect becomes obvious by comparing Fig. 3 (c) with Fig. 3 (d). The latter figure shows the band structure for magnetization along [0 0 1]. Out of the five apparent band crossings marked in Fig. 3 (c), two are now visibly split. Those, (2) and (4), are marked in parentheses in Fig. 3 (d). Moreover, six new apparent crossings manifest themselves, marked with letters a to f.

Fig. 3 (e, f) show comparisons between GGA and GGA+OPC band structures. OPC does in general not change the symmetry of bands that are already subject to spin-orbit and exchange splittings. However, it can considerably enhance the existing splittings in proportion to the local orbital moments. Here, related band shifts up to several 10 meV are observed in the vicinity of the Fermi level. The effect of OPC on band crossings is of quantitative nature for  $M||$  [1 0 0], Fig. 3 (e), but disappearance of the degeneracies d and e by the action of OPC is observed for  $M||$  [0 0 1], Fig. 3 (f). Below, we will study the effect of OPC on the target quantity of this work, the AHC.

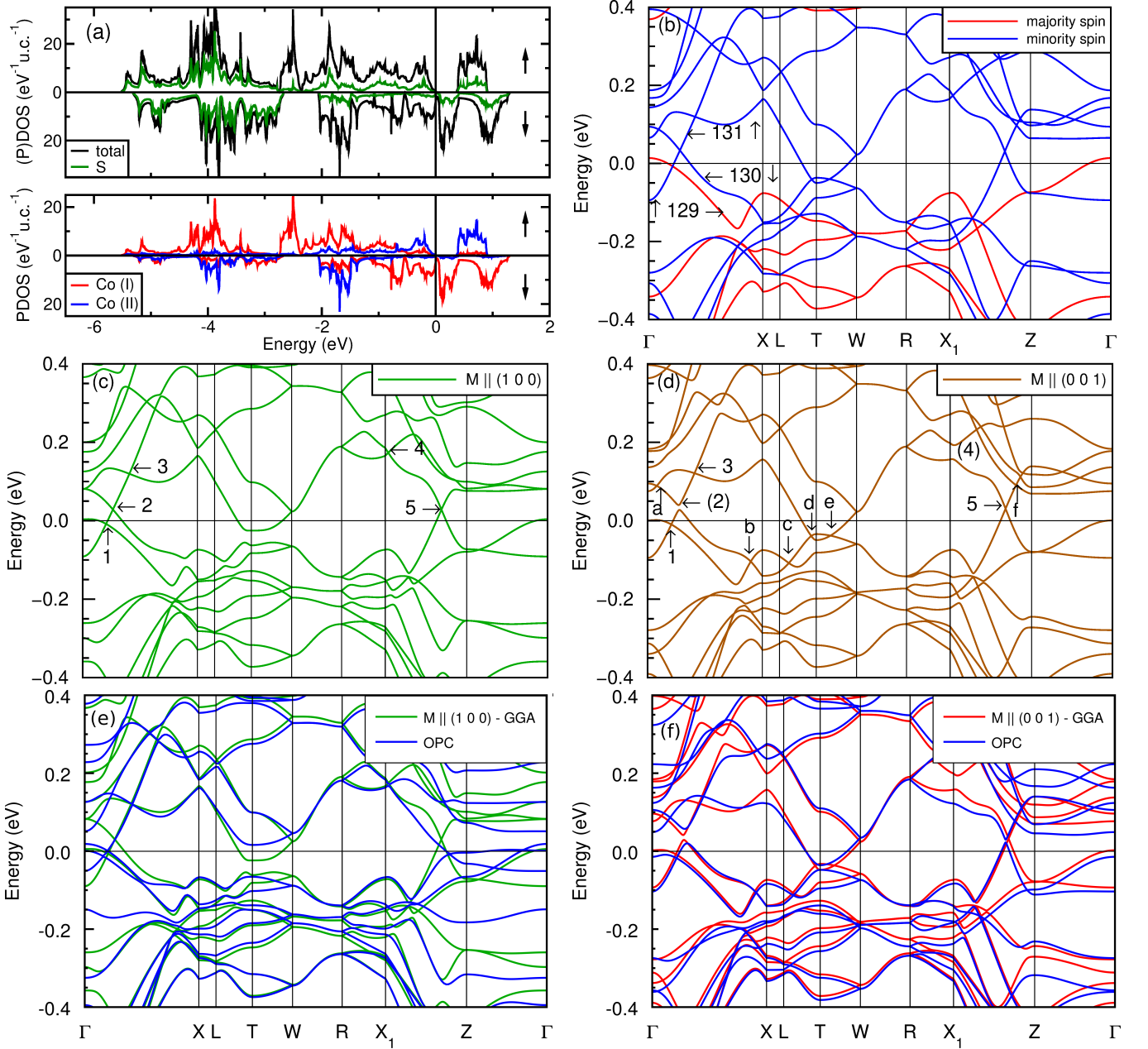


FIG. 3. Electronic structure of the ground state magnetic configuration. The Fermi level is set to zero energy in all sub-figures and indicated with solid lines. (a) Total and partial DOS obtained in scalar relativistic mode. The majority and minority spin channels are indicated by up- and down-arrows, respectively. The total DOS is shown with black lines, the partial sulphur, Cobalt(I), and Cobalt(II) contributions with green, red, and blue lines, respectively. (b) Electronic band structure obtained in scalar relativistic mode. The majority and minority spin contributions are shown with red and blue lines, respectively. Several numbers of bands close to the Fermi level are given together with arrows pointing to the related bands. Note, the numbering is in the order of the band energy at each  $k$ -point. (c) Electronic band structure obtained in full relativistic mode with magnetization  $M$  parallel to  $[1\ 0\ 0]$  (ground state). Apparent band crossings involving bands  $n$  and  $n+1$ ,  $n = \{129, 130, 131\}$ , are indicated with arrows and numbered. (d) Electronic band structure obtained in full relativistic mode with magnetization  $M$  parallel to  $[0\ 0\ 1]$ . Apparent band crossings involving bands  $n$  and  $n+1$ ,  $n = \{129, 130, 131\}$ , are indicated with arrows. Crossings already present for  $M$  parallel to  $[1\ 0\ 0]$  are numbered as before; former crossings that are obviously gapped are numbered with parentheses; new crossings are distinguished by letters. (e, f) Comparison between electronic band structures in full relativistic mode with magnetization  $M$  parallel to  $[1\ 0\ 0]$  and  $[0\ 0\ 1]$ , respectively, obtained with GGA (same data as in (c, d)) and with GGA+OPC.

### C. WEYL POINTS

We are now going to clarify the character of the apparent band crossings found in the previous section and to

investigate their dependence on the direction of magneti-

zation. For this aim, sets of Weyl points were searched using the Wannier presentation of the DFT band structure among all bands  $n$  and  $n + 1$ ,  $n = \{129, 130, 131\}$ . For comparison, or if the visible crossing was not detected as a Weyl point while using the search algorithm, additional checks using the DFT band structure were performed.

Tab. IV shows the results for the ground state with  $M \parallel [1\ 0\ 0]$ . For this orientation of  $M$ , the magnetic point group includes a simple (i.e., without time reversal)  $C_2(x)$  rotation axis. All five apparent crossings lie on this axis, including points 4 and 5 which can be shifted to a position with  $k_y = k_z = 0$  by subtracting a reciprocal lattice vector. Along any simple  $C_2$  axis, crossings between bands belonging to the two different irreps are always WPs. [63, 65] All five points are indeed confirmed as WPs with chiralities  $\chi$  of 1 or -1. Their energies and  $k_x$ -positions obtained from the Wannier Hamiltonian are close to the related DFT results.

TABLE IV. Characteristics of points in the low-energy electronic structure of  $\text{Cs}_2\text{Co}_3\text{S}_4$ , if the magnetization points along the  $[1\ 0\ 0]$  direction. “P” denotes the specific points as defined in Fig. 3 (c);  $E$  is the energy relative to the Fermi level;  $k_i$ , ( $i = x, y, z$ ) are the coordinates of one representative position of the point set; “M” is the symmetry-determined multiplicity of the positions; “T” is the type of the node (WP: confirmed Weyl point);  $\chi$  is the chirality. Energies and positions obtained from the DFT calculation are given in parentheses.

P	E[meV]	$k_x[2\pi/a]$	$k_y[2\pi/b]$	$k_z[2\pi/c]$	M	T	$\chi$
1	-6 (-8)	0.118 (0.119)	0 (0)	0 (0)	2	WP	1
2	32 (28)	0.153 (0.154)	0 (0)	0 (0)	2	WP	-1
3	123 (120)	0.236 (0.238)	0 (0)	0 (0)	2	WP	1
4	179 (173)	0.399 (0.400)	0 (0)	1 (1)	2	WP	-1
5	33 (28)	0.132 (0.129)	0 (0)	1 (1)	2	WP	1

If the magnetization is rotated away from the easy  $[1\ 0\ 0]$  axis, the electronic structure changes. As a consequence, the Weyl points move both in energy and position. [44, 63] Tab. V and Tab. VI show, how the angle  $\phi$  of magnetization, varied in steps of 15 degrees from  $[1\ 0\ 0]$  toward  $[0\ 0\ 1]$ , affects point 2 and point 5, respectively. We note, that the band energy  $E$  and  $k_x$  are only marginally shifted. However, the WPs move strongly in the direction of  $k_z$  in both cases. For  $M \parallel [M_x\ 0\ M_z]$ ,  $M_z \neq 0$ , the  $m'_z$  plane (mirror plane with time reversal) is not contained in the magnetic point group, in distinction to  $M \parallel [1\ 0\ 0]$ . Thus, for  $\phi \neq 0$ , the multiplicity of the WPs does not depend on  $k_z$ . Especially,  $k_z = 0$  is not a plane with a symmetry different from  $k_z \neq 0$ . Vice versa, a set of WPs with multiplicity 2 and coordinates  $(k_x, 0, k_z \neq 0)$  for the case of  $M \parallel [M_x\ 0\ M_z]$ ,  $M_z \neq 0$ , has to move toward the plane  $k_z = 0$  if  $M$  rotates toward

$[1\ 0\ 0]$  in order to keep its multiplicity.

If  $\phi$  exceeds 45 degrees, none of the WP pairs can be detected. Obviously, they are annihilated before  $\phi$  reaches the value of 60 degrees.

TABLE V. Impact of magnetization direction on the WP number 2.  $\phi$  denotes the deflection of the magnetization direction from  $[1\ 0\ 0]$  toward  $[0\ 0\ 1]$ , in degree;  $E$  is the energy relative to the Fermi level;  $k_i$ , ( $i = x, y, z$ ) are the coordinates of one representative position of the WP set; “M” is the symmetry-determined multiplicity of the positions. Note, the data for  $\phi = 0$  are the same as given in Tab. IV

$\phi$	E[meV]	$k_x[2\pi/a]$	$k_y[2\pi/b]$	$k_z[2\pi/c]$	M
0	32	0.153	0	0	2
15	31	0.153	0	0.076	2
30	31	0.154	0	0.179	2
45	30	0.155	0	0.339	2

TABLE VI. Impact of magnetization direction on the WP number 5.  $\phi$  denotes the deflection of the magnetization direction from  $[1\ 0\ 0]$  toward  $[0\ 0\ 1]$ , in degree;  $E$  is the energy relative to the Fermi level;  $k_i$ , ( $i = x, y, z$ ) are the coordinates of one representative position of the WP set; “M” is the symmetry-determined multiplicity of the positions. Note, the data for  $\phi = 0$  are the same as given in Tab. IV

$\phi$	E[meV]	$k_x[2\pi/a]$	$k_y[2\pi/b]$	$k_z[2\pi/c]$	M
0	33	0.132	0	1	2
15	31	0.134	0	0.898	2
30	31	0.135	0	0.851	2
45	30	0.142	0	0.691	2

The magnetic point group changes again, if the magnetization direction reaches  $[0\ 0\ 1]$ . In this case,  $m(z)$  becomes a simple mirror plane, and the same holds for the equivalent plane  $k_z = 2\pi/c$ . Such a plane cannot host WPs, since the chiral charge is odd under reflection, and the generic degeneracies are nodal lines. [63] Indeed, we found only one WP among the apparent degeneracies (point e), see Tab. VII. Another WP (point g, which is not on a symmetry line) was found during the general search. As required by symmetry, the two WPs e and g are not situated on a mirror plane. Two of the other apparent degeneracies were found to be gapped (point 3, point 5). The remaining six degeneracies, which all are located on a mirror plane, were identified as points on a nodal line. A comparison between the Wannier data and the DFT results for the degenerate points shows, that the related band energies almost agree. This holds as well for the  $k_x$  and  $k_y$  coordinates, while the values for  $k_z$  deviate somewhat stronger from each other.



TABLE VII. Characteristics of points in the low-energy electronic structure of  $\text{Cs}_2\text{Co}_3\text{S}_4$ , if the magnetization points along the  $[0\ 0\ 1]$  direction. “P” denotes the specific points as defined in Fig. 3 (d) and one more point, g, which is not situated on a symmetry line;  $E$  is the energy relative to the Fermi level;  $k_i$ , ( $i = x, y, z$ ) are the coordinates of one representative position of the point set; “M” is the symmetry-determined multiplicity of the positions; “T” is the type of the point (WP: confirmed Weyl point; NL: a point on a nodal line; G: gapped);  $\chi$  is the chirality in case of a confirmed Weyl point. Energies and positions obtained from the DFT calculation are given in parentheses.

P	E[meV]	$k_x[2\pi/a]$	$k_y[2\pi/b]$	$k_z[2\pi/c]$	M	T	$\chi$
a	92 (89)	0.043 (0.047)	0 (0)	0 (0)	2	NL	
1	-9 (-10)	0.120 (0.121)	0 (0)	0 (0)	2	NL	
3	123 (121)	0.237 (0.239)	0 (0)	0 (0)	2	G	
b	-104 (-104)	0.527 (0.526)	0 (0)	0 (0)	2	NL	
c	-109 (-108)	0.563 (0.563)	0.254 (0.255)	0 (0)	4	NL	
d	-38 (-39)	0.510 (0.511)	0.460 (0.456)	0 (0)	4	NL	
e	-36 (-38)	0.5 (0.5)	0.5 (0.5)	0.140 (0.176)	4	WP	-1
5	34 (31)	0.136 (0.133)	0 (0)	1 (1)	2	G	
f	91 (90)	0.084 (0.080)	0 (0)	1 (1)	2	NL	
g	35 (35)	0.863 (0.865)	0 (0)	0.112 (0.141)	4	WP	-1

#### D. ANOMALOUS HALL CONDUCTIVITY

The anomalous Hall effect (AHE) is a notable characteristic of magnetic materials. Three particular contributions to the anomalous Hall conductivity (AHC),  $\sigma_{xy}^{\text{an}}$  are commonly distinguished: the intrinsic contribution,  $\sigma_{xy}^{\text{an,in}}$ , which arises solely from the material’s band structure, the skew scattering contribution  $\sigma_{xy}^{\text{an,sk}}$ , and the side jump contribution  $\sigma_{xy}^{\text{an,sj}}$ . The latter two arise from extrinsic mechanisms. [66] All three contributions are additive,  $\sigma_{xy}^{\text{an}} = \sigma_{xy}^{\text{an,in}} + \sigma_{xy}^{\text{an,sk}} + \sigma_{xy}^{\text{an,sj}}$ . Here, we consider only the intrinsic contribution to the AHC, which is known to reach large values in magnetic WSMs. [41, 67–70] This behavior is considered to be due to the non-trivial band topology at WPs with related large Berry curvature  $\Omega(k)$ . As  $k$ -space analogy to magnetic dipoles, pairs of WPs act as sources and sinks of Berry curvature which, in turn, generates the AHC.

The Kubo-formula linear-response approach was used to evaluate the AHC from the Berry curvature, [71] based on the available tight-binding Hamiltonian:

$$\sigma_{ab}^{\text{an,in}} = -\frac{e^2}{\hbar} \sum_{n,c} \epsilon_{abc} \int_{\text{BZ}} \frac{d^3k}{(2\pi)^3} f_0(E_n(k)) \Omega_n^c(k), \quad (1)$$

where  $\epsilon_{abc}$  is the Levi-Civita tensor,  $f_0(E_n(k))$  is the equilibrium Fermi-Dirac distribution function,  $n$  is the band index,  $E_n(k)$  is the related eigenvalue at  $k$ , and  $\Omega_n^c$  is the  $c$ -component of the Berry curvature.

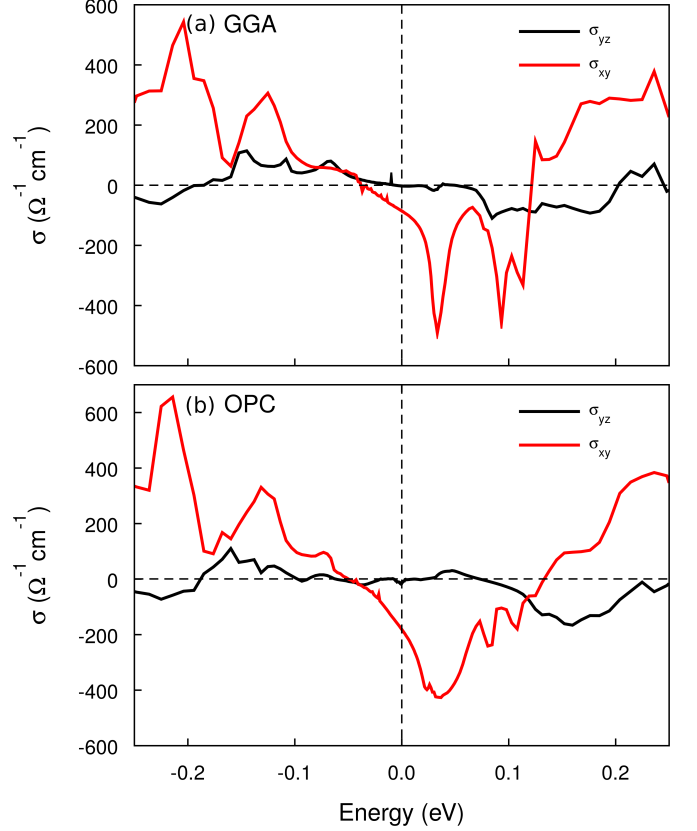


FIG. 4. Intrinsic anomalous Hall conductivity of  $\text{Cs}_2\text{Co}_3\text{S}_4$  as a function of the chemical potential. The AHC  $\sigma_{yz}$  and  $\sigma_{xy}$  were obtained for magnetization directions along  $[100]$  and  $[001]$ , within (a) GGA and (b) GGA+OPC, respectively.

Fig. 4 (a, b) shows the band-intrinsic contribution to the AHC as a function of the chemical potential and the magnetization direction, obtained with a zero-temperature Fermi-Dirac distribution function, computed within GGA and GGA+OPC functionals. For the two considered magnetization directions  $[100]$  and  $[001]$ ,  $\sigma_{yz}^{\text{an,in}}$  and  $\sigma_{xy}^{\text{an,in}}$ , respectively, were evaluated. Roughly, the shape and magnitude of AHC is similar for the two approximations used. A closer inspection shows that the AHC obtained with GGA is more structured than that one obtained with GGA+OPC. We attribute this difference to the additional  $k$ -dependent band splittings produced by OPC.

In the ground state with easy magnetization axis  $[100]$ , the calculated AHC is found to be nearly zero at  $E_F$ , but finite with  $\sim -15$  (27)  $\Omega^{-1}\text{cm}^{-1}$  around 30 meV above  $E_F$  within GGA (GGA+OPC), where four WPs were found. However, this feature is much less prominent than the extended regions of large  $|\sigma_{yz}^{\text{an,in}}|$  farther away from the Fermi level. These regions may originate from WPs that were not found in our limited search described in the



previous section. However, it is known that in general the combination of broken time reversal symmetry with spin-orbit coupling generates contributions to the AHC also for bands with zero Chern number. [72] Thus, the relation between AHC and Weyl points can be relatively weak, as already observed, e.g., in Ref. 44.

For the [001] direction of magnetization, on the other hand, the calculated AHC at  $E_F$  amounts to -86 (-184)  $\Omega^{-1}\text{cm}^{-1}$  within GGA (GGA+OPC). At around 30 meV above  $E_F$ , a prominent AHC peak is observed with a magnitude of  $\sim 500$  (430)  $\Omega^{-1}\text{cm}^{-1}$ , appearing at the position of the observed WP (point g). It is worth noting that, with a small amount of electron doping, a large value of AHC can be attained at  $E_F$ .

#### IV. SUMMARY

To summarize, we investigated the electronic structure, the magnetic properties, and the intrinsic contributions to the anomalous Hall effect of  $\text{Cs}_2\text{Co}_3\text{S}_4$  by means of density-functional theory calculations. We found a ferromagnetic ground state of the title compound, at variance with the original experimental results that report an antiferromagnetic low-temperature state. The energy difference between the two states is in the order of meV/atom. Thus, a very small off-stoichiometry of the samples could have influenced the experimental result; likewise, one should keep in mind the limitations of the chosen approximations to the density functional.

We characterized the theoretical ground state as a semi-metal that is very close to a half-metallic state. Several Weyl points are situated close to the Fermi level for the lowest-energy orientation of magnetization along [1 0 0]. They move both in  $k$  and energy if the magnetization is rotated and are eventually annihilated. Related, we found the intrinsic anomalous Hall conductivity to be very sensitive to the orientation of the magnetization. It is relatively small for the easy-axis orientation but reaches magnitudes up to 500  $\Omega^{-1}\text{cm}^{-1}$  if the magnetization is oriented along [0 0 1].

Further experimental efforts on this interesting, though scarcely investigated system are encouraged.

#### ACKNOWLEDGMENTS

This work was supported by a grant from UNESCO-TWAS and the Swedish International Development Cooperation Agency (SIDA) (award no. 21-377 RG/PHYS/AS.G). The views expressed herein do not necessarily represent those of UNESCO-TWAS, SIDA or its Board of Governors. M.P.G. acknowledges the Alexander von Humboldt Foundation, Germany for the equipment grants and IFW-Dresden for providing large-scale compute nodes to Tribhuvan University for scientific computations. M.P.G. thanks the University

Grants Commission, Nepal for the Collaborative Research Grants (award no. CRG-78/79 S&T-03). G.B.A. thanks Nepal Academy of Science and Technology for the PhD fellowship. All authors thank Ulrike Nitzsche for her skillful technical assistance.

#### Appendix A: Gauge choice for link variables

The Berry phase  $\gamma = \oint \mathbf{A} d\mathbf{k}$  collected along a closed loop encircling a nodal line is an odd multiple of  $\pi$ . The well known discretization [73]  $\gamma = i \sum_{i=0}^{N-1} \ln \langle u^{\mathbf{k}_i} | u^{\mathbf{k}_{i+1} \bmod N} \rangle$  of this integral ( $u^{\mathbf{k}}$  is the periodic part of the wave function  $\Psi^{\mathbf{k}}$ ) contains the link variable  $U^{\mathbf{k}_i} = \langle u^{\mathbf{k}_i} | u^{\mathbf{k}_{i+1} \bmod N} \rangle$ , which can be generalized to the multi band case [74] to safely handle degeneracies.

We used such integrals based on an FPLO Wannier model to prove the existence of nodal lines in our compound.

To complement the discussion in Ref. 62 of the proper approximation to a neglected position operator contribution to the Berry connection we will show the corresponding choice for link variables.

For a Wannier model one has wave function  $\Psi_n^{\mathbf{k}} = (\Phi^{\mathbf{k}} C^{\mathbf{k}})_n = \sum_{\mathbf{s}\mu} \Phi_{\mathbf{s}\mu}^{\mathbf{k}} C_{\mathbf{s}\mu,n}^{\mathbf{k}}$  of band  $n$  with Bloch sums  $\Phi_{\mathbf{s}\mu}^{\mathbf{k}}$  of Wannier functions at site  $\mathbf{s}$  with quantum numbers  $\mu$ . The Berry connection matrix then has two terms, one containing the basis connection matrix  $\mathbf{A}_{\Phi}^{\mathbf{k}} = \langle \Phi^{\mathbf{k}+} | \beta_{\mathbf{k}} \Phi^{\mathbf{k}} \rangle$  (with Berry operator  $\beta_{\mathbf{k}} = e^{i\mathbf{k}\mathbf{r}} i \nabla_{\mathbf{k}} e^{-i\mathbf{k}\mathbf{r}}$ ) and a coefficient term

$$\mathbf{A}_{\Psi}^{\mathbf{k}} = C^{\mathbf{k}+} \mathbf{A}_{\Phi}^{\mathbf{k}} C^{\mathbf{k}} + C^{\mathbf{k}+} S^{\mathbf{k}} i \nabla_{\mathbf{k}} C^{\mathbf{k}}$$

where  $S^{\mathbf{k}} = \langle \Phi^{\mathbf{k}} | \Phi^{\mathbf{k}} \rangle$  is the overlap matrix (for generality). While the basis connection  $\mathbf{A}_{\Phi}^{\mathbf{k}}$  is related to the position operator in Wannier basis, in models one does not know that term. Hence, for simplification or for model situations an approximation of  $\mathbf{A}_{\Phi}^{\mathbf{k}}$  is needed. It was shown in Ref. 62 that a simple approximation  $\mathbf{A}_{\Phi,s's'}^{\mathbf{k}} = \bar{\lambda} S_{s's}^{\mathbf{k}} \mathbf{s}$  (with  $\mathbf{s}$  and  $\mathbf{s}'$  being site vectors) yields proper crystal symmetry of all results. It depends on the choice of the gauge of the Bloch sums  $\Phi_s^{\mathbf{k}\lambda}(\mathbf{r}) = \frac{1}{\sqrt{N}} \sum_{\mathbf{R}} e^{i\mathbf{k}(\mathbf{R}+\lambda\mathbf{s})} \Phi_s(\mathbf{r}-\mathbf{R}-\mathbf{s})$ . For periodic gauge  $\bar{\lambda} = 1 - \lambda = 1$  and for relative gauge  $\bar{\lambda} = 0$ , which implies that the latter yields the simplest formulas.

In the context of link variables this will also lead to modifications. Calculating the full expression and using the approximation for the basis connection we get for infinitesimally close  $\mathbf{k}$ -points (hiding  $\mathbf{s}$  and  $\mu$  sums)

$$\begin{aligned} \langle u^{\mathbf{k}} | u^{\mathbf{k}+\mathbf{h}} \rangle &= \left\langle e^{-i\mathbf{k}\mathbf{r}} \Psi^{\mathbf{k}} \middle| e^{-i(\mathbf{k}+\mathbf{h})\mathbf{r}} \Psi^{\mathbf{k}+\mathbf{h}} \right\rangle \\ &\approx \langle \Psi^{\mathbf{k}+} | e^{i\mathbf{k}\mathbf{r}} (1 - i i (\mathbf{h} \nabla_{\mathbf{k}})) e^{-i\mathbf{k}\mathbf{r}} \Psi^{\mathbf{k}} \rangle \\ &= 1 - i \langle \Phi^{\mathbf{k}+} | \beta_{\mathbf{k}} \Phi^{\mathbf{k}} \rangle \mathbf{h} \\ &= 1 - i C^{\mathbf{k}+} (\bar{\lambda} S^{\mathbf{k}} \mathbf{s} + i \nabla_{\mathbf{k}}) C^{\mathbf{k}} \mathbf{h} \end{aligned}$$

Dropping the basis connection is equivalent to replacing  $\langle u^{\mathbf{k}} | u^{\mathbf{k}+\mathbf{h}} \rangle$  by  $D^{\mathbf{k}+\mathbf{G}} D^{\mathbf{k}}$  with an appropriately chosen  $D^{\mathbf{k}} = \varphi^{\mathbf{k}} C^{\mathbf{k}}$  containing a phase factor  $\varphi^{\mathbf{k}}$ .

For topology a periodic wave function  $\Psi^{\mathbf{k}+\mathbf{G}} = \Psi^{\mathbf{k}}$  is required. In detail for the Bloch sums  $\Phi_s^{\mathbf{k}+\mathbf{G},\lambda} = \Phi_s^{\mathbf{k},\lambda} e^{i\mathbf{G}\lambda s}$  and periodicity requires  $C_{sn}^{\mathbf{k}+\mathbf{G}} = e^{-i\mathbf{G}\lambda s} C_{sn}^{\mathbf{k}}$ : whenever a wave vector  $\mathbf{k} + \mathbf{G}$  occurs in an algorithm for which  $C_{sn}^{\mathbf{k}}$  is already in use one needs to use  $e^{-i\mathbf{G}\lambda s} C_{sn}^{\mathbf{k}}$  instead of  $C_{sn}^{\mathbf{k}+\mathbf{G}}$ .

From Ref. 62 we know that the relative gauge  $\bar{\lambda} = 0$  leads to vanishing approximations for  $\mathbf{A}_{\Phi}^{\mathbf{k}}$  and hence we choose  $\varphi_s^{\mathbf{k}} = e^{-i\mathbf{k}\bar{\lambda}s}$ , since then  $\Phi_s^{\mathbf{k},\lambda} = \Phi_s^{\mathbf{k},\bar{\lambda}=0} \varphi_s^{\mathbf{k}}$  and we are allowed to drop  $\Phi_s^{\mathbf{k},\bar{\lambda}=0}$  (which is in relative gauge). Consequently we need to modify  $C_{s\mu,n}^{\mathbf{k}} \rightarrow D_{s\mu,n}^{\mathbf{k}} = e^{-i\mathbf{k}\bar{\lambda}s} C_{s\mu,n}^{\mathbf{k}}$  when calculating link variables from coefficient matrices only. For orthogonal  $\Phi^{\mathbf{k}}$  ( $S^{\mathbf{k}} = 1$ ) one

gets ( $s, \mu$ -sum implied)

$$D^{\mathbf{k}+\mathbf{G}} D^{\mathbf{k}} = D_{s\mu,n'}^{\mathbf{k}+\mathbf{G}} D_{s\mu,n}^{\mathbf{k}+\mathbf{h}} = C_{s\mu,n'}^{\mathbf{k}+\mathbf{G}} e^{-i\mathbf{h}\bar{\lambda}s} C_{s\mu,n}^{\mathbf{k}+\mathbf{h}} \\ \approx 1 - i C_{s\mu,n'}^{\mathbf{k}+\mathbf{G}} (\bar{\lambda}s + i\nabla_{\mathbf{k}}) C_{s\mu,n}^{\mathbf{k}} \mathbf{h}$$

which is the same as derived above. In conclusion we suggest to either use the relative gauge  $\bar{\lambda} = 0$  or the additional phase factor when calculating link variables based on coefficient matrices only.

## AUTHOR CONTRIBUTIONS

G.B.A. performed DFT calculations, Wannier mapping and search for Weyl points, and wrote the first draft of the manuscript; M.R. performed DFT calculations and revised the manuscript; K.K. wrote the Appendix and provided the code for the calculation of the Berry phase on a closed loop. M.P.G. planned the project, performed DFT and AHC calculations and revised the manuscript. All authors proof-read the manuscript.

- 
- [1] J. Zou, Z. He, and G. Xu, *Npj Comput. Mater.* **5**, 96 (2019).
  - [2] J. E. Moore, *Nature* **464**, 194 (2010).
  - [3] L. Fu, C. L. Kane, and E. J. Mele, *Phys. Rev. Lett.* **98**, 106803 (2007).
  - [4] M. Z. Hasan and C. L. Kane, *Rev. Mod. Phys.* **82**, 3045 (2010).
  - [5] Y. Tokura, K. Yasuda, and A. Tsukazaki, *Nat. Rev. Phys.* **1**, 126 (2019).
  - [6] M. Z. Hasan and J. E. Moore, *Annu. Rev. Condens. Matter Phys.* **2**, 55 (2011).
  - [7] H. Gao, J. W. Venderbos, Y. Kim, and A. M. Rappe, *Annu. Rev. Mater. Res.* **49**, 153 (2019).
  - [8] H. Weng, X. Dai, and Z. Fang, *J. Condens. Matter Phys.* **28**, 303001 (2016).
  - [9] M. Kang, L. Ye, S. Fang, J.-S. You, A. Levitan, M. Han, J. I. Facio, C. Jozwiak, A. Bostwick, E. Rotenberg, *et al.*, *Nat. Mater.* **19**, 163 (2020).
  - [10] L. Ye, M. K. Chan, R. D. McDonald, D. Graf, M. Kang, J. Liu, T. Suzuki, R. Comin, L. Fu, and J. G. Checkelsky, *Nat. Commun.* **10**, 1 (2019).
  - [11] N. P. Armitage, E. J. Mele, and A. Vishwanath, *Rev. Mod. Phys.* **90**, 015001 (2018).
  - [12] W. Yu, W. Pan, D. L. Medlin, M. A. Rodriguez, S. R. Lee, Z.-q. Bao, and F. Zhang, *Phys. Rev. Lett.* **120**, 177704 (2018).
  - [13] M. Hirayama, R. Okugawa, and S. Murakami, *Journal of the JPSJ* **87**, 041002 (2018).
  - [14] B. Q. Lv, T. Qian, and H. Ding, *Rev. Mod. Phys.* **93**, 025002 (2021).
  - [15] A. Bansil, H. Lin, and T. Das, *Rev. Mod. Phys.* **88**, 021004 (2016).
  - [16] B. Zheng, B. Xia, R. Wang, J. Zhao, Z. Chen, Y. Zhao, and H. Xu, *Npj Comput. Mater.* **5**, 1 (2019).
  - [17] H. Nielsen and M. Ninomiya, *Nucl. Phys. B.* **185**, 20 (1981).
  - [18] H. Nielsen and M. Ninomiya, *Nucl. Phys. B.* **193**, 173 (1981).
  - [19] P. Hosur and X. Qi, *Comptes Rendus Physique* **14**, 857 (2013), topological insulators / Isolants topologiques.
  - [20] D. Bulmash, C.-X. Liu, and X.-L. Qi, *Phys. Rev. B* **89**, 081106 (2014).
  - [21] H. Weng, C. Fang, Z. Fang, B. A. Bernevig, and X. Dai, *Phys. Rev. X* **5**, 011029 (2015).
  - [22] B. Q. Lv, H. M. Weng, B. B. Fu, X. P. Wang, H. Miao, J. Ma, P. Richard, X. C. Huang, L. X. Zhao, G. F. Chen, Z. Fang, X. Dai, T. Qian, and H. Ding, *Phys. Rev. X* **5**, 031013 (2015).
  - [23] I. Belopolski, S.-Y. Xu, D. S. Sanchez, G. Chang, C. Guo, M. Neupane, H. Zheng, C.-C. Lee, S.-M. Huang, G. Bian, N. Alidoust, T.-R. Chang, B. Wang, X. Zhang, A. Bansil, H.-T. Jeng, H. Lin, S. Jia, and M. Z. Hasan, *Phys. Rev. Lett.* **116**, 066802 (2016).
  - [24] A. A. Soluyanov, D. Gresch, Z. Wang, Q. Wu, M. Troyer, X. Dai, and B. A. Bernevig, *Nature* **527**, 495 (2015).
  - [25] P. Li, Y. Wen, X. He, Q. Zhang, C. Xia, Z.-M. Yu, S. A. Yang, Z. Zhu, H. N. Alshareef, and X.-X. Zhang, *Nat. Commun.* **8**, 1 (2017).
  - [26] Y. Sun, S.-C. Wu, M. N. Ali, C. Felser, and B. Yan, *Phys. Rev. B* **92**, 161107 (2015).
  - [27] K. Deng, G. Wan, P. Deng, K. Zhang, S. Ding, E. Wang, M. Yan, H. Huang, H. Zhang, Z. Xu, *et al.*, *Nat. Phys.* **12**, 1105 (2016).
  - [28] A. Tamai, Q. S. Wu, I. Cucchi, F. Y. Bruno, S. Riccò, T. K. Kim, M. Hoesch, C. Barreateau, E. Giannini, C. Besnard, A. A. Soluyanov, and F. Baumberger, *Phys. Rev. X* **6**, 031021 (2016).
  - [29] T.-R. Chang, S.-Y. Xu, G. Chang, C.-C. Lee, S.-M. Huang, B. Wang, G. Bian, H. Zheng, D. S. Sanchez, I. Belopolski, *et al.*, *Nat. Commun.* **7**, 1 (2016).
  - [30] I. Belopolski, D. S. Sanchez, Y. Ishida, X. Pan, P. Yu, S.-Y. Xu, G. Chang, T.-R. Chang, H. Zheng, N. Alidoust,

- et al.*, Nat. Commun. **7**, 1 (2016).
- [31] I. Belopolski, S.-Y. Xu, Y. Ishida, X. Pan, P. Yu, D. S. Sanchez, H. Zheng, M. Neupane, N. Alidoust, G. Chang, T.-R. Chang, Y. Wu, G. Bian, S.-M. Huang, C.-C. Lee, D. Mou, L. Huang, Y. Song, B. Wang, G. Wang, Y.-W. Yeh, N. Yao, J. E. Rault, P. Le Fèvre, F. m. c. Bertran, H.-T. Jeng, T. Kondo, A. Kaminski, H. Lin, Z. Liu, F. Song, S. Shin, and M. Z. Hasan, Phys. Rev. B **94**, 085127 (2016).
  - [32] B. Karki, B. P. Belbase, G. B. Acharya, S. Singh, and M. P. Ghimire, Phys. Rev. B **105**, 125138 (2022).
  - [33] E. Haubold, K. Koepernik, D. Efremov, S. Khim, A. Fedorov, Y. Kushnirenko, J. van den Brink, S. Wurmehl, B. Büchner, T. K. Kim, M. Hoesch, K. Sumida, K. Taguchi, T. Yoshikawa, A. Kimura, T. Okuda, and S. V. Borisenko, Phys. Rev. B **95**, 241108 (2017).
  - [34] X. Zhou, Q. Liu, Q. Wu, T. Nummy, H. Li, J. Griffith, S. Parham, J. Waugh, E. Emmanouilidou, B. Shen, O. V. Yazyev, N. Ni, and D. Dessau, Phys. Rev. B **97**, 241102 (2018).
  - [35] S. Wang, B.-C. Lin, A.-Q. Wang, D.-P. Yu, and Z.-M. Liao, Advances in Physics: X **2**, 518 (2017).
  - [36] B.-C. Lin, S. Wang, L.-X. Wang, C.-Z. Li, J.-G. Li, D. Yu, and Z.-M. Liao, Phys. Rev. B **95**, 235436 (2017).
  - [37] P. Baireuther, J. Tworzydło, M. Breitzkreiz, İ. Adagideli, and C. W. J. Beenakker, New J. Phys. **19**, 025006 (2017).
  - [38] A.-Q. Wang, C.-Z. Li, C. Li, Z.-M. Liao, A. Brinkman, and D.-P. Yu, Phys. Rev. Lett. **121**, 237701 (2018).
  - [39] X. Wan, A. M. Turner, A. Vishwanath, and S. Y. Savrasov, Phys. Rev. B **83**, 205101 (2011).
  - [40] G. Xu, H. Weng, Z. Wang, X. Dai, and Z. Fang, Phys. Rev. Lett. **107**, 186806 (2011).
  - [41] W. Shi, L. Muechler, K. Manna, Y. Zhang, K. Koepernik, R. Car, J. van den Brink, C. Felser, and Y. Sun, Phys. Rev. B **97**, 060406 (2018).
  - [42] N. Morali, R. Batabyal, P. K. Nag, E. Liu, Q. Xu, Y. Sun, B. Yan, C. Felser, N. Avraham, and H. Beidenkopf, Science **365**, 1286 (2019).
  - [43] I. Belopolski, K. Manna, D. S. Sanchez, G. Chang, B. Ernst, J. Yin, S. S. Zhang, T. Cochran, N. Shumiya, H. Zheng, *et al.*, Science **365**, 1278 (2019).
  - [44] M. P. Ghimire, J. I. Facio, J.-S. You, L. Ye, J. G. Checkelsky, S. Fang, E. Kaxiras, M. Richter, and J. van den Brink, Phys. Rev. Res. **1**, 032044 (2019).
  - [45] S. Borisenko, D. Evtushinsky, Q. Gibson, A. Yaresko, K. Koepernik, T. Kim, M. Ali, J. van den Brink, M. Hoesch, A. Fedorov, *et al.*, Nat. Commun. **10**, 1 (2019).
  - [46] K. Kuroda, T. Tomita, M.-T. Suzuki, C. Bareille, A. Nugroho, P. Goswami, M. Ochi, M. Ikhlas, M. Nakayama, S. Akebi, *et al.*, Nat. Mater. **16**, 1090 (2017).
  - [47] A. K. Nayak, J. E. Fischer, Y. Sun, B. Yan, J. Karel, A. C. Komarek, C. Shekhar, N. Kumar, W. Schnelle, J. Kübler, *et al.*, Sci. Adv. **2**, e1501870 (2016).
  - [48] M. Hirschberger, S. Kushwaha, Z. Wang, Q. Gibson, S. Liang, C. A. Belvin, B. A. Bernevig, R. J. Cava, and N. P. Ong, Nat. Mater. **15**, 1161 (2016).
  - [49] J. Kübler and C. Felser, EPL **114**, 47005 (2016).
  - [50] Z. Wang, M. G. Vergniory, S. Kushwaha, M. Hirschberger, E. V. Chulkov, A. Ernst, N. P. Ong, R. J. Cava, and B. A. Bernevig, Phys. Rev. Lett. **117**, 236401 (2016).
  - [51] S. K. Kushwaha, Z. Wang, T. Kong, and R. J. Cava, J. Condens. Matter Phys. **30**, 075701 (2018).
  - [52] R. Ray, B. Sadhukhan, M. Richter, J. I. Facio, and J. van den Brink, npj Quantum Mater. **7**, 1 (2022).
  - [53] W. Bronger and P. Böttcher, Z. Anorg. Allg. Chem. **390**, 1 (1972).
  - [54] W. Bronger, U. Hendriks, and P. Müller, Z. Anorg. Allg. Chem. **559**, 95 (1988).
  - [55] K. Koepernik and H. Eschrig, Phys. Rev. B **59**, 1743 (1999).
  - [56] J. P. Perdew, K. Burke, and M. Ernzerhof, Phys. Rev. Lett. **77**, 3865 (1996).
  - [57] F. Zhou and V. Ozoliņš, Phys. Rev. B **80**, 125127 (2009).
  - [58] L. Nordström, M. S. S. Brooks, and B. Johansson, J. Phys.: Cond. Matter **4**, 3261 (1992).
  - [59] P. Blaha, K. Schwarz, G. K. Madsen, D. Kvasnicka, J. Luitz, *et al.*, An augmented plane wave+ local orbitals program for calculating crystal properties **60**, 155 (2001).
  - [60] F. Tran and P. Blaha, Phys. Rev. B Condens. **83**, 235118 (2011).
  - [61] K. Schwarz and P. Mohn, J. Phys. F **14**, L129 (1984).
  - [62] K. Koepernik, O. Janson, Y. Sun, and J. van den Brink, Physical Review B **107**, 235135 (2023).
  - [63] D. Gosálbez-Martínez, I. Souza, and D. Vanderbilt, Phys. Rev. B **92**, 085138 (2015).
  - [64] H. Eschrig, M. Sargolzaei, K. Koepernik, and M. Richter, EPL **72**, 611 (2005).
  - [65] C. Fang, M. J. Gilbert, X. Dai, and B. A. Bernevig, Phys. Rev. Lett. **108**, 266802 (2012).
  - [66] N. Nagaosa, J. Sinova, S. Onoda, A. H. MacDonald, and N. P. Ong, Rev. Mod. Phys. **82**, 1539 (2010).
  - [67] E. Liu, Y. Sun, N. Kumar, L. Muechler, A. Sun, L. Jiao, S.-Y. Yang, D. Liu, A. Liang, Q. Xu, *et al.*, Nat. Phys. **14**, 1125 (2018).
  - [68] K. Manna, L. Muechler, T.-H. Kao, R. Stinchhoff, Y. Zhang, J. Gooth, N. Kumar, G. Kreiner, K. Koepernik, R. Car, J. Kübler, G. H. Fecher, C. Shekhar, Y. Sun, and C. Felser, Phys. Rev. X **8**, 041045 (2018).
  - [69] D. Chen, C. Le, C. Fu, H. Lin, W. Schnelle, Y. Sun, and C. Felser, Phys. Rev. B **103**, 144410 (2021).
  - [70] S. Fang, L. Ye, M. P. Ghimire, M. Kang, J. Liu, M. Han, L. Fu, M. Richter, J. van den Brink, E. Kaxiras, R. Comin, and J. G. Checkelsky, Phys. Rev. B **105**, 035107 (2022).
  - [71] N.-N. Zhao, K. Liu, and Z.-Y. Lu, Phys. Rev. B **103**, 205104 (2021).
  - [72] D. Xiao, M.-C. Chang, and Q. Niu, Rev. Mod. Phys. **82**, 1959 (2010).
  - [73] R. D. King-Smith and D. Vanderbilt, Physical Review B **47**, 1651 (1993).
  - [74] T. Fukui, Y. Hatsugai, and H. Suzuki, Journal of the Physical Society of Japan **74**, 1674 (2005).